CHIN. PHYS. LETT. Vol. 38, No. 2 (2021) 027301

Directional Design of Materials Based on Multi-Objective Optimization: A Case Study of Two-Dimensional Thermoelectric SnSe

Shenshen Yan(闫申申)[1], Yi Wang(汪毅)[1], Zhibin Gao(高志斌)[1,2], Yang Long(龙洋)[1], and Jie Ren(任捷)[1,3*]

[1]*Center for Phononics and Thermal Energy Science, China-EU Joint Lab on Nanophononics, Shanghai Key Laboratory of Special Artificial Microstructure Materials and Technology, School of Physics Science and Engineering, Tongji University, Shanghai 200092, China*

[2]*Department of Physics, National University of Singapore, Singapore 117551, Republic of Singapore*

[3]*Shanghai Research Institute for Intelligent Autonomous Systems, Tongji University, Shanghai 200092, China*

(Received 9 November 2020; accepted 14 December 2020; published online 27 January 2021)

The directional design of functional materials with multi-objective constraints is a big challenge, in which performance and stability are determined by a complicated interconnection of different physical factors. We apply multi-objective optimization, based on the Pareto Efficiency and Particle-Swarm Optimization methods, to design new functional materials directionally. As a demonstration, we achieve the thermoelectric design of 2D SnSe materials via the above methods. We identify several novel metastable 2D SnSe structures with simultaneously lower free energy and better thermoelectric performance in their experimentally reported monolayer structures. We hope that the results of our work on the multi-objective Pareto Optimization method will represent a step forward in the integrative design of future multi-objective and multi-functional materials.

DOI: 10.1088/0256-307X/38/2/027301

Thermoelectric devices and materials are capable of directly converting electricity into thermal energy for cooling, or generating electrical power from waste heat, indicating their great potential for reducing environmental pollution and providing cleaner energy. Moreover, the Seebeck effect can generate electrical power from waste heat, as described by the Seebeck thermopower coefficient, $S = -\Delta V/\Delta T$, where ΔV is the voltage potential, and ΔT is the temperature difference.[1] Thermopower plays an important role in thermoelectric materials.

Recently, the discovery of bulk tin selenide (SnSe), with the capacity to undergo a second-order phase transition from a low symmetry *Pnma* to a high symmetry *Cmcm* phase at 810 K, has highlighted the significance of thermoelectric materials, primarily due to its ultralow thermal conductivity and ultrahigh power factor.[2,3] This outstanding material has rapidly aroused widespread attention in various fields, including theoretical exploration[4–8] and experimental study.[9–15] It has a great potential with respect to the study of thermoelectric properties,[16] in addition to representing a bright prospect for the future development of novel thermoelectric materials. Although some degree of controversy surrounds this single-crystalline SnSe sample and its measured thermal conductivity,[17] these seminal works have made a crucial step toward increased thermoelectric performance in simple and pure bulk materials without need for doping or phononic crystals. Moreover, Nishimura *et al.*[18] revealed the convergency of new Fermi pockets in an SnSe *Pnma* structure at about 0.89 GPa. Due to the quantum confinement effect, two-dimensional (2D) materials possess some unexpected properties, as compared with their pristine bulk counterparts.[19–21]

Furthermore, the discovery of these materials, and the use of machine learning strategies to explore material design[22,23] have made remarkable progress. Recently, the clustering and inverse design of topological materials achieved via machine learning have been applied in both phononic[24] and photonic[25] materials. As the same time, the application of machine learning strategies could pave the way to the discovery and design of additional high-performance thermoelectric materials.[26,27] Several monolayer SnSe structures have recently been discovered.[28–30] In the context of such innovation, it is worth exploring these novel stable 2D SnSe materials with high thermopower. However, simultaneously satisfying the two objectives of stability and performance in terms of generating electrical power from waste heat represents a multi-objective optimization problem.

In the mapping from structure to function, microscopic atomic configuration is at the core of macroscopic properties. Owing to significant developments

Supported by the National Natural Science Foundation of China (Grant Nos. 11935010 and 11775159), the Shanghai Science and Technology Committee (Grant Nos. 18ZR1442800 and 18JC1410900), and the Opening Project of Shanghai Key Laboratory of Special Artificial Microstructure Materials and Technology.

*Corresponding author. Email: Xonics@tongji.edu.cn

© 2021 Chinese Physical Society and IOP Publishing Ltd

in crystalline structure prediction, new materials can be inversely searched by artificial intelligence, such as the Genetic Algorithm (GA),[31] Particle Swarm Optimization (PSO),[32] rather than the traditional, more costly Edisonian trial-and-error approach. These metastable structures are of great importance, and may exhibit high-performance characteristics.[33,34] Multiple objective algorithms[35,36] have been applied to deal more efficiently with the multi-objective problem. The multi-objective Particle Swarm Optimization (MOPSO) algorithm, for example, is simple to implement with relatively few hyper-parameters. Moreover, it also achieves a faster convergence rate for global or local optima via sharing information between particles.[37–39] Research has been undertaken to search for novel atomic SiO_2 monolayers with a negative Poisson ratio,[20] and HfO_2 monolayers with a high static dielectric constant[40] via multi-objective optimization, which combines first-principles calculations with GA.

In this Letter, we adopt the MOPSO-sigma algorithm,[35] which is efficient and reliable, to directionally design 2D SnSe materials with lower free energy and increased thermopower, based on Pareto optimality. In this process, Pareto fronts are obtained via the fast non-dominated sorting approach.[41]

During the design process using the MOPSO algorithm, self-consistent energy calculations and structural optimization were employed, using the Perdew–Burke–Ernzerhof (PBE) exchange-correlation functional[42] alongside projector-augmented wave (PAW) potentials[43] implemented using the Vienna *ab initio* simulation package (VASP).[44] The energy convergence threshold is set to 10^{-4} eV, and all the atoms are allowed to relax until the maximal Hellmann–Feynman force is below 0.001 eV/Å. Following this process, in order to obtain accurate results with respect to crystal structure, band structure, thermopower, and phonon dispersion, we reset the energy convergence threshold and maximal Hellmann–Feynman force to 10^{-8} eV and 10^{-6} eV/Å. The kinetic energy cut-off was 500 eV, and phonon dispersion was obtained using the Phonopy package.[45] The Seebeck coefficient was evaluated using BoltzTraP,[46] and the multi-objective method based on the Pareto optimality[47,48] discussed here has been implemented via our homemade computer code.

The workflow of directional design for the thermoelectric materials based on Pareto optimality is shown in Fig. 1(b). Firstly, the initial crystal structures are generated through the atomic Wyckoff position and 230 space groups, and similar structures are removed in order to avoid wasting computational resources.[32] Next, local optimization (structure relaxation) is utilized sequentially to eliminate some of the worst structures. This crucial process guarantees population diversity and gives the whole energy landscape in a well-organized shape. Thirdly, two objectives, free energy and thermopower are calculated. Here, as a benchmark, we only consider the data for thermopower at room temperature (300 K) in all our calculations. The next pivotal step is to apply a multi-objective method to design structures with lower free energy and a higher Seebeck coefficient, based on Pareto optimality. In contrast to any other single objective optimization algorithm, the leader is not one structure with unique properties, but a leader set, known as the Pareto front, which includes structures with lower free energy and greater thermopower. Generally, in a collection of 2D SnSe materials, $\{M_n\} = \{M_1, \ldots M_i, \ldots M_j, \ldots M_N\}$, $n \in \{1, 2, \ldots, N\}$, N is the number of all structures. If M_i possesses lower free energy and greater thermopower than M_j, this means that M_j is dominated by M_i, and M_i is a non-dominated solution of M_j, as per the following equations: $E(M_i) \leq E(M_j)$; and $S(M_i) \geq S(M_j)$, where the $E(M_i)$ and $S(M_i)$ denote the free energy and thermopower of structure M_i, respectively.

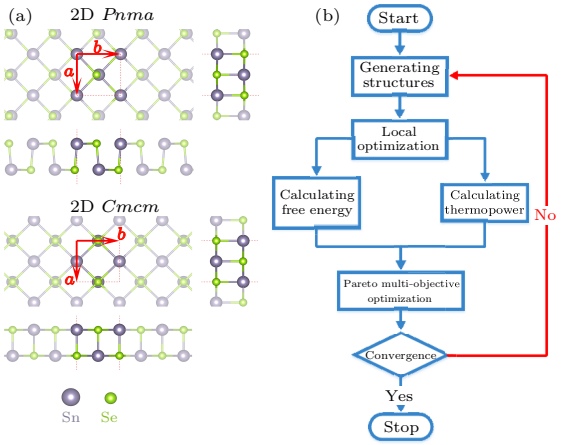

Fig. 1. (a) Three-view drawings of two typical 2D SnSe structures, corresponding to monolayers of the *Pnma* and *Cmcm* bulk phases. The dark gray and green atom symbols denote Sn and Se, respectively. (b) Workflow of the directional design for 2D SnSe materials, based on Pareto multi-objective optimization.

If a given S_i is not dominated by any others, then S_i is regarded as a Pareto optimality or Pareto efficiency structure. All the Pareto optimality structures constitute the Pareto front. We then apply the PSO algorithm to make the Pareto front lead all the population structures forward to the next Pareto front[35] with lower free energy and larger thermopower. Finally, if the convergence criterion is reached, the whole procedure will stop and output the reasonable Pareto front. Otherwise, return and repeat all the above processes.

The result of adopting multi-objectives is shown

in Fig. 2(a), which includes 2700 samples in the process to design stable functional structures, based only on chemical composition. For example, there are only first three Pareto fronts highlighted in Fig. 2(a). The red line represents the first Pareto front, set inherently with respect to those structures with the lowest free energy and larger thermopower, represented by circles. Interestingly, we find known 2D SnSe structures,[4,49] denoted by violet rhombus symbols, and their left nearest neighbor (gray dashed circles) corresponding to the 2D *Pnma* and 2D *Cmcm* structures of SnSe shown in Fig. 1(a), respectively, during our blind searching processes, which tends to validate the correctness and exhibit the robustness of our multi-objective design method. Furthermore, as shown in Fig. 2(b), we note four novel monolayer materials with superior stability and much greater thermopower than the known structures in Fig. 1(a), specifically SnSe-I, SnSe-Ⅱ, SnSe-Ⅲ and SnSe-Ⅳ, denoted by the orange hexagon, magenta square, yellow pentagram, and green triangle on the first Pareto front, respectively. Here, we focus only on monolayer structures, and ignore the bilayer phases. The bilayer phases correspond to the blue hollow hexagons on the first Pareto front, as shown in the Supporting Information. Moreover, the light blue circles with blue dashed line and the light cyan circles with cyan dashed line represent the second and third Pareto fronts, respectively. The monolayer of the Cmcm phase is also found, represented by the light blue circle with dotted circle lying on the second Pareto front. Additional structures on the second and third Pareto fronts are shown in the Supporting Information, including quasi-one dimensional, bilayer and novel metastable atomic configurations. The grey circles represent the dominant structures with much higher free energy and lower thermopower than the first three Pareto fronts, and are not discussed in this study.

The structure of the orange hexagon, SnSe-I, is that of a honeycomb monolayer, similar to silicene,[50] with small buckling from one side view. The blue hollow hexagons denote the bilayer counterparts of the honeycomb structures. SnSe-Ⅲ, the yellow pentagram, is the structure with armchair and zigzag ridges from the different side views. In addition, we discovered accidentally that the same main group and stoichiometric number of GeSe have been synthesized by high-pressure techniques,[51] whose one layer is very similar to the structure of SnSe-Ⅲ. The structure of the magenta square, SnSe-Ⅱ, is a combination of cells of SnSe-I and SnSe-Ⅲ. More interestingly, we also find that another structure, SnSe-Ⅳ, indicated by a green triangle, comprises cells of the monolayer of *Pnma* and SnSe-I. The optimized structural properties of the novel 2D SnSe structures are summarized in Table 1.

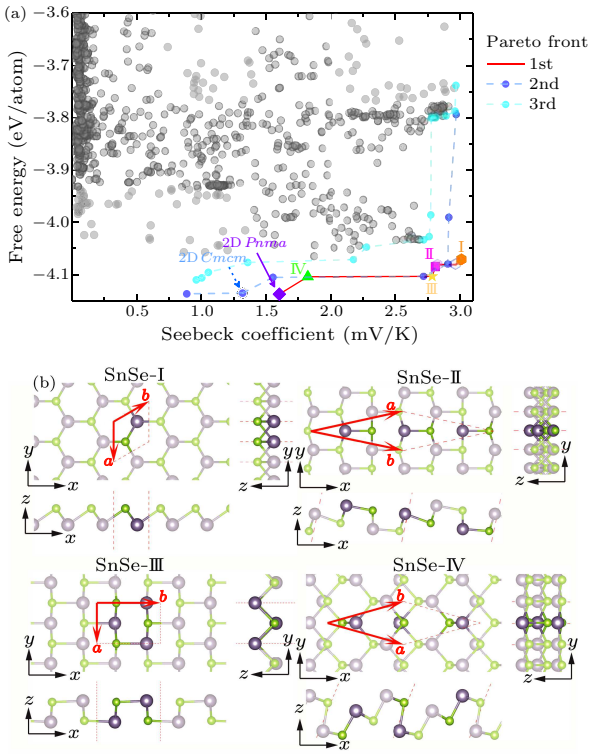

Fig. 2. Thermopower landscape at room temperature (300 K) versus the free energy of 2D SnSe materials and monolayer structures on the first Pareto front. (a) The red line denotes the first Pareto front; the larger colorful symbols represent monolayer structures with simultaneously larger Seebeck coefficients and lower free energy than others, all represented by circles. The light blue circles with blue dashed line, and the light cyan circles with cyan dashed line denote the second and third Pareto fronts, respectively. The grey circles are the dominant structures in the first three Pareto fronts. The violet rhombus and the near light blue circle with dotted circle denote the monolayers of the *Pnma* phase and the *Cmcm* phase, respectively. (b) Three views of four new monolayer structures on the first Pareto front, SnSe-I, SnSe-Ⅱ, SnSe-Ⅲ and SnSe-Ⅳ, corresponding to the orange hexagon, magenta square, yellow pentagram, and green triangle in (a), respectively. The blue hollow hexagons on the first Pareto front correspond to the bilayer SnSe structures discussed in the Supporting Information.

Next, we confirm the thermoelectric performance and stability of the novel 2D SnSe structures on the first Pareto front, which have light higher free energy and much larger thermopower than the structures in Fig. 1(a), using the multi-objective method. The first priority is to certify the stability of these new free-standing 2D SnSe materials. The free energy of SnSe-I (−4.079 eV/atom), SnSe-Ⅱ (−4.091 eV/atom), SnSe-Ⅲ (−4.103 eV/atom), and SnSe-Ⅳ (−4.106 eV/atom) are all higher than free energy of the *Pnma* phase (−4.137 eV/atom). The dynamical stabilities of these metastable structures have been confirmed by phonon dispersion relations at 0 K, and *ab initio* molecular dynamics (AIMD) simulations at 300 K, as shown in Figs. 3(a) and 3(b). There is no imaginary frequency in the phonon dispersions of the 2D SnSe-I, SnSe-

Ⅲ, or SnSe-Ⅳ. Moreover, there are a few imaginary frequencies near the Γ point in the phonon dispersion of 2D SnSe-Ⅱ. For 2D materials, these imaginary frequencies near the Γ point have also been reported for germanene,[50] as well as honeycomb arsenenes,[52] and this artificial imprecision in the computation has nothing to do with structural transition or instability.[53–55] Subsequent to the AIMD and NVT ensemble simulations, the atomic configurations are altered to the position of equilibrium at 300 K. Furthermore, AIMD simulations with NVE ensemble at a series of elevated temperatures with a lifetime of 9 ps at 300 K are performed, in order to verify their dynamic stability with the oscillating free energy shown in Fig. 3(b). The top views of 2D SnSe-I, SnSe-Ⅱ, SnSe-Ⅲ, and SnSe-Ⅳ after the AIMD simulations are shown in the inset pictures. These illustrate the dynamic stability of the four structures.

Table 1. Properties of four 2D SnSe structures. Here, a and b are the lattice parameters. The E, $m^*_{\mathrm{DOS,F}}$, m^*_{band}, N_v, and S denote free energy per atom, density-of-states effective mass at the Fermi energy level, isotropic parabolic band effective mass, band degeneracy, and thermopower, respectively, where m_{e} is the free electron mass.

Materials	Space group (No.)	a (Å)	b (Å)	E (eV/atom)	m^*_{band} (m_{e})	$m^*_{\mathrm{DOS,F}}$ (m_{e})	N_v	S (mV/K)
SnSe-I	$P3m1$ (156)	3.91	3.91	−4.08	1.34	8.03	6	3.587
SnSe-Ⅱ	Cm (8)	9.64	9.64	−4.09	2.19	4.38	2	2.763
SnSe-Ⅲ	$Pmmn$ (59)	3.92	6.17	−4.10	1.31	2.62	2	2.596
SnSe-Ⅳ	Cm (8)	7.67	7.67	−4.11	0.37, 0.76	1.13	2	1.871

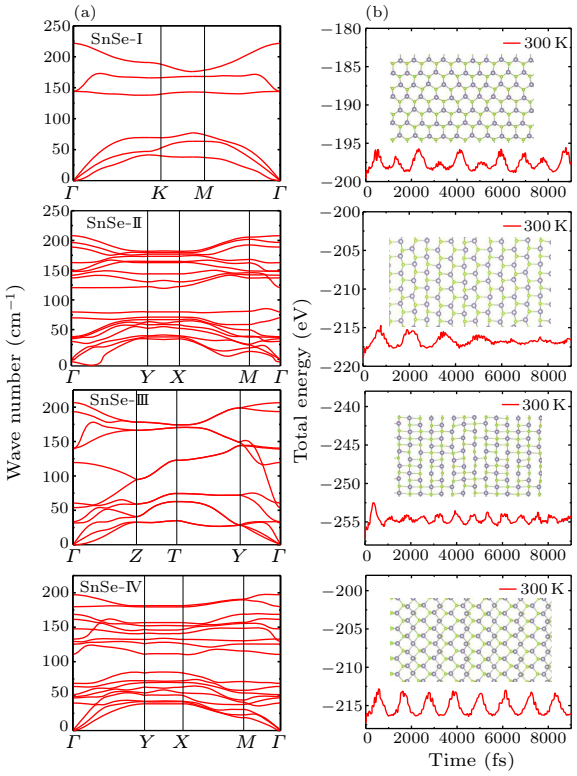

Fig. 3. Phonon dispersions and AIMD simulations at 300 K of SnSe-I, SnSe-Ⅱ, SnSe-Ⅲ, and SnSe-Ⅳ. (a) Phonon dispersions along the high symmetry points. There is no imaginary frequency in the phonon dispersions of SnSe-I, SnSe-Ⅲ, and SnSe-Ⅳ, and there are few imaginary frequencies near the Γ point in the phonon dispersion of SnSe-Ⅱ. (b) The total energy varies with time during the AIMD simulations at 300 K with a lifetime of 9 ps. The oscillating redlines represent the changes of the total free energy during the AIMD simulations. The inset pictures of AIMD simulations are the top views of SnSe-I, SnSe-Ⅱ, SnSe-Ⅲ, and SnSe-Ⅳ structures after the AIMD simulations, respectively.

The electronic band structure-linked density of states (DOS), Fermi surface, and thermopower of SnSe-I, SnSe-Ⅱ, SnSe-Ⅲ, and SnSe-Ⅳ, are shown in Fig. 4. We find that in the SnSe-I structure, the valence band maximum (VBM) is in the Γ–K path, and the conduction band minimum (CBM) is in the M–Γ path in the Brillouin zone (BZ), with an indirect band gap of 2.22 eV. In the case of SnSe-Ⅱ, the VBM is in the Y–Γ path, and the CBM is in the Γ point, with an indirect band gap of 1.66 eV. For SnSe-Ⅲ, the VBM is in the Y–Γ path, and the CBM is in the Γ–Z path, with an indirect band gap of 1.61 eV. Furthermore, with respect to SnSe-Ⅳ, both VBM and CBM are in the Γ point, with a direct band gap of 1.10 eV. Their band gaps are all larger than that of the monolayer $Pnma$ phase (0.91 eV[4]). In all four structures, the sharp peaks of DOS near the valence maxima and conduction minima may enhance their thermopower value.

Figure 4(c) shows the average thermopower, depending on chemical potential. The thermopower along the x and y directions is shown in the Supporting Information. The positive and negative signs of thermopower correspond to the hole carrier (p-type and $\mu < 0$) and the electron carrier (n-type and $\mu > 0$), respectively. The maximum thermopower with p-type carrier concentrations of SnSe-I, SnSe-Ⅱ, SnSe-Ⅲ, and SnSe-Ⅳ are 3.587 mV/K, 2.763 mV/K, 2.596 mV/K, and 1.871 mV/K, which are much greater than the values for the known 2D SnSe monolayer in the $Pnma$ phase [around 1.75 mV/K],[56] and 3–6 times that of bulk SnSe [0.5-0.58 mV/K].[57]

Generally speaking, there are several approaches to enhance thermopower, including high valley degeneracy produced by carrier pocket engineering,[8,13,14,18,58,59] a distorted DOS, via dop-

ing, to resonate one energy level of a localized atom,[60] weak electron-phonon coupling,[61] the phonon drag effect,[62] and a pudding-mold-like shape in the highest valence band or lowest conduction band, which is beneficial to a high Seebeck coefficient value and high conductivity.[63] In the Mott formula,[64] $S = \frac{\pi^2 k_B^2 T}{3q} \frac{d[\ln[\sigma(E)]]}{dE}|_{E=E_F}$, where $\sigma(E) = g(E)f(E)q\mu$ is the energy-dependent electrical conductivity. Meanwhile, $\sigma(E)$ is dominated by $f(E)$, $g(E)$, q, k_B, and μ, i.e., the Fermi–Dirac distribution function, the DOS, the carrier charge, the Boltzmann constant, and mobility, respectively. Generally, where materials exhibit a substantial local increase in the energy-dependent DOS at the Fermi energy, the thermopower will be significantly enhanced.

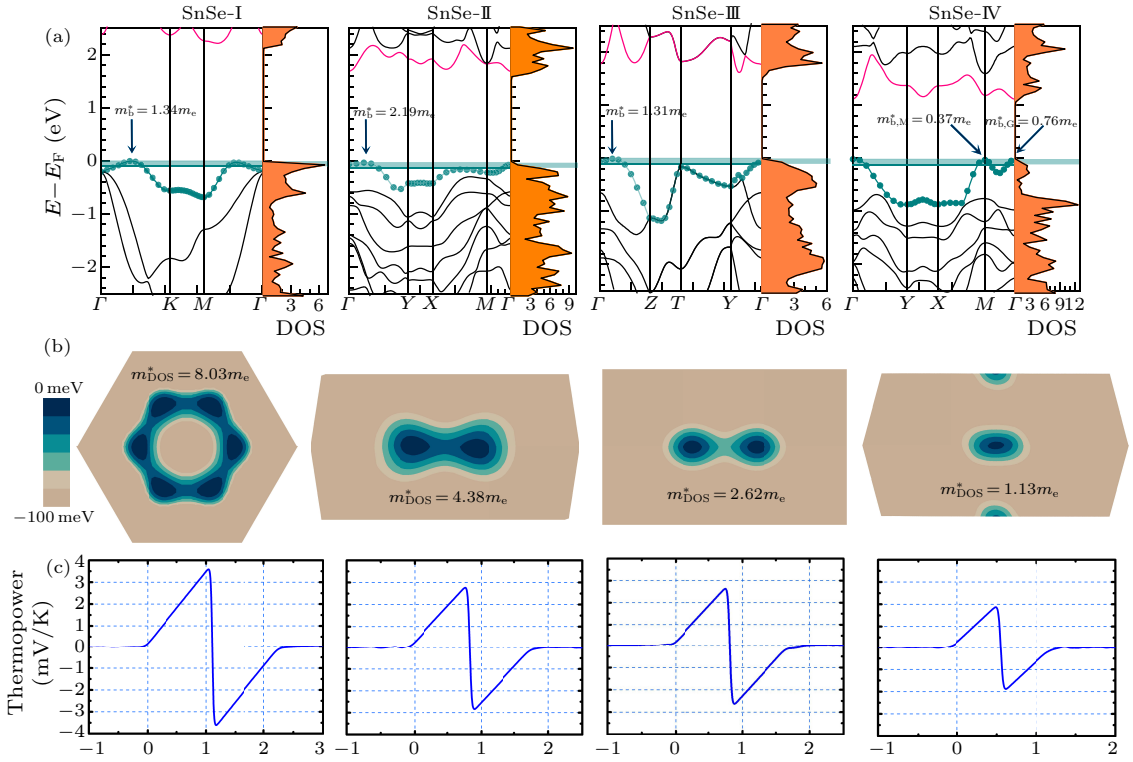

Fig. 4. Electronic band structure-linked density of states (DOS), Fermi surface, and thermopower of SnSe-I, Ⅱ, Ⅲ, Ⅳ. (a) Electronic band structure linked DOS. the cyan line and symbol are the valence band falling on the 100 meV energy window of the VCM, denoted by the cyan flat band. The Fermi energy is set to 0 eV. (b) Fermi surface in the first Brillouin zone in the 100 meV energy window of the VCM, corresponding to the cyan flat band in (a). (c) Average Seebeck coefficient versus chemical potential.

For 2D materials, the correlation between the thermopower and the DOS effective mass at the Fermi energy can be expressed by the following equation (details can be found in the Supporting Information): in contrast to the thermopower of 3D materials, $S_{3D} = \frac{2\pi^2 k_B^2 T}{3q\hbar^2}(\frac{1}{3\pi^2 n})^{2/3} m_{DOS,F}^*$, for 2D materials, $S_{2D} = \frac{\pi k_B^2 T}{6qn\hbar^2} m_{DOS,F}^*$, where $\hbar$ is the reduced Planck's constant, $m_{DOS,F}^*$ is the DOS effective mass at the Fermi energy level, and n is the carrier concentration. Therefore, larger DOS effective mass will lead to greater thermopower.

For 2D materials, the correlation between the DOS effective mass (m_{DOS}^*) and the isotropic parabolic band effective mass (m_{band}^*) is

$$m_{DOS}^* = N_v m_{band}^*, \tag{1}$$

in contrast to the formula for 3D density-of-states effective mass: $m_{DOS} = N_v^{2/3} m_{band}$, where the N_v is the band degeneracy (details can be found in the Supporting Information). In the sense of p-type doping, the Fermi energy is close to the top of the valence band, and Fermi surfaces within 100 meV from the top of the valence band in the first Brillouin zone are calculated, as shown in Fig. 4(b). Based on the electronic band structures and Fermi surfaces of the SnSe-I, SnSe-Ⅱ, SnSe-Ⅲ, and SnSe-Ⅳ structures, we find that the values of band degeneracy N_v are 6, 2, 2, 2, and that the DOS effective mass (the isotropic parabolic band effective mass) values are $8.03m_e$ ($1.34m_e$), $4.38m_e$ ($2.19m_e$), $2.62m_e$ ($1.31m_e$), $1.13m_e$ ($0.37m_e$ at M point and $0.76m_e$ at G point), respectively, where m_e is the free electron mass.

According to the Mott formula, together with the DOS effective mass of 2D materials, we can directly

obtain the thermopower measurement for 2D materials:

$$S_{2D} = N_v m^*_{band} \frac{\pi k_B^2 T}{6qn\hbar^2}, \quad (2)$$

which differs from the thermopower calculation for 3D materials: $S_{3D} = N_v^{2/3} m^*_{band} \frac{2\pi^2 k_B^2 T}{3q\hbar^2} (\frac{1}{3\pi^2 n})^{2/3}$. Here, thermopower is determined by band degeneracy N_v, band effective mass m^*_{band} and carrier concentration n. In addition, the band degeneracy in 2D materials is more important than in 3D materials with respect to thermopower. For the four 2D SnSe materials, the higher band degeneracy and band effective mass could lead to the larger density-of-states effective mass m^*_{DOS}, as well as the higher thermopower, as shown in Table 1. Due to the different correlations between thermopower and band degeneracy, $S_{2D} \propto N_v$ for 2D materials and $S_{3D} \propto N_v^{2/3}$ for 3D materials, the band degeneracy N_v plays a more vital role in the case of 2D materials. Moreover, the band engineering strategies[58,65–67] have the capacity to increase the band degeneracy of 3D materials, which would be even more effective for 2D materials.

In conclusion, we have achieved the directional design of materials via the multi-objective Pareto optimization method, based on Pareto efficiency and particle-swarm optimization only, in accordance with chemical composition. This method facilitates the design of structures with lower free energy and greater thermopower at the same time. The designed novel 2D SnSe monolayers on the first Pareto front also indicate that structures from main groups Ⅳ–Ⅵ, for instance, the monolayer of β-GeSe at the high pressure,[51] and main group-V, such as abundant phosphorene,[68–70] may share similar homogeneous configurations, owing to their similar outer valence electrons. Hence, the efficiency of Pareto optimization of structures has demonstrated that it is instructive with respect to materials design, and even for the purpose of experimental synthesis.

So far, we have only focused on stability and thermopower. Moreover, we explain why the band degeneracy is more significant in relation to thermopower in 2D materials than in 3D materials. In the future, we will apply more functional objectives, such as electronic relaxation time and lattice thermal conductivity, to the design of efficient thermoelectric materials, possibly even to the design of multiple-function materials.

References

[1] Bell L E 2008 *Science* **321** 1457
[2] Zhao L D, Lo S H, Zhang Y, Sun H, Tan G, Uher C, Wolverton C, Dravid V P and Kanatzidis M G 2014 *Nature* **508** 373
[3] Zhao L D, Tan G, Hao S, He J, Pei Y, Chi H, Wang H, Gong S, Xu H, Dravid V P, Uher C, Snyder G J, Wolverton C and Kanatzidis M G 2016 *Science* **351** 141
[4] Wang F Q, Zhang S, Yu J and Wang Q 2015 *Nanoscale* **7** 15962
[5] Bansal D, Hong J, Li C W, May A F, Porter W, Hu M Y, Abernathy D L and Delaire O 2016 *Phys. Rev. B* **94** 054307
[6] Mehboudi M, Fregoso B M, Yang Y, Zhu W, van der Zande A, Ferrer J, Bellaiche L, Kumar P and Barraza-Lopez S 2016 *Phys. Rev. Lett.* **117** 246802
[7] Skelton J M, Burton L A, Parker S C, Walsh A, Kim C E, Soon A, Buckeridge J, Sokol A A, Catlow C R A, Togo A *et al.* 2016 *Phys. Rev. Lett.* **117** 075502
[8] Zhang K, Deng K, Li J, Zhang H, Yao W, Denlinger J, Wu Y, Duan W and Zhou S 2018 *Phys. Rev. Mater.* **2** 054603
[9] Li L, Chen Z, Hu Y, Wang X, Zhang T, Chen W and Wang Q 2013 *J. Am. Chem. Soc.* **135** 1213
[10] Zhang C, Yin H, Han M, Dai Z, Pang H, Zheng Y, Lan Y Q, Bao J and Zhu J 2014 *ACS Nano* **8** 3761
[11] Zhao S, Wang H, Zhou Y, Liao L, Jiang Y, Yang X, Chen G, Lin M, Wang Y, Peng H *et al.* 2015 *Nano Res.* **8** 288
[12] Chang C, Wu M, He D, Pei Y, Wu C F, Wu X, Yu H, Zhu F, Wang K, Chen Y, Huang L, Li J F, He J and Zhao L D 2018 *Science* **360** 778
[13] Wang Z, Fan C, Shen Z, Hua C, Hu Q, Sheng F, Lu Y, Fang H, Qiu Z, Lu J *et al.* 2018 *Nat. Commun.* **9** 47
[14] Qin B, Wang D, He W, Zhang Y, Wu H, Pennycook S J and Zhao L D 2019 *J. Am. Chem. Soc.* **141** 1141
[15] Burton M R, Mehraban S, Beynon D, McGettrick J, Watson T, Lavery N P and Carnie M J 2019 *Adv. Energy Mater.* **9** 1900201
[16] Chen Z G, Shi X, Zhao L D and Zou J 2018 *Prog. Mater. Sci.* **97** 283
[17] Wei P C, Bhattacharya S, He J, Neeleshwar S, Podila R, Chen Y and Rao A 2016 *Nature* **539** E1
[18] Nishimura T, Sakai H, Mori H, Akiba K, Usui H, Ochi M, Kuroki K, Miyake A, Tokunaga M, Uwatoko Y, Katayama K, Murakawa H and Hanasaki N 2019 *Phys. Rev. Lett.* **122** 226601
[19] Xu X, Pereira L F, Wang Y, Wu J, Zhang K, Zhao X, Bae S, Bui C T, Xie R, Thong J T *et al.* 2014 *Nat. Commun.* **5** 3689
[20] Gao Z, Dong X, Li N and Ren J 2017 *Nano Lett.* **17** 772
[21] Shimizu S, Bahramy M S, Iizuka T, Ono S, Miwa K, Tokura Y and Iwasa Y 2016 *Proc. Natl. Acad. Sci. USA* **113** 6438
[22] Schmidt J, Marques M R G, Botti S and Marques M A L 2019 *npj Comput. Mater.* **5** 83
[23] Gubernatis J E and Lookman T 2018 *Phys. Rev. Mater.* **2** 120301
[24] Long Y, Ren J and Chen H 2020 *Phys. Rev. Lett.* **124** 185501
[25] Long Y, Ren J, Li Y and Chen H 2019 *Appl. Phys. Lett.* **114** 181105
[26] Hao S, Dravid V P, Kanatzidis M G and Wolverton C 2019 *npj Comput. Mater.* **5** 58
[27] Iwasaki Y, Takeuchi I, Stanev V, Kusne A G, Ishida M, Kirihara A, Ihara K, Sawada R, Terashima K, Someya H, Uchida K I, Saitoh E and Yorozu S 2019 *Sci. Rep.* **9** 2751
[28] Hu Z Y, Li K Y, Lu Y, Huang Y and Shao X H 2017 *Nanoscale* **9** 16093
[29] Ul H B, AlFaify S, Ahmed R, Butt F K, Laref A and Shkir M 2018 *Phys. Rev. B* **97** 075438
[30] Ul H B, AlFaify S and Laref A 2019 *Phys. Chem. Chem. Phys.* **21** 4624
[31] Oganov A R and Glass C W 2006 *J. Chem. Phys.* **124** 244704
[32] Wang Y, Lv J, Zhu L and Ma Y 2010 *Phys. Rev. B* **82** 094116
[33] Kappera R, Voiry D, Yalcin S E, Branch B, Gupta G, Mo-

hite A D and Chhowalla M 2014 *Nat. Mater.* **13** 1128
[34] Cho S, Kim S, Kim J H, Zhao J, Seok J, Keum D H, Baik J, Choe D H, Chang K J, Suenaga K, Kim S W, Lee Y H and Yang H 2015 *Science* **349** 625
[35] Mostaghim S and Teich J 2003 *Proceedings of the 2003 IEEE Swarm Intelligence Symposium* SIS'03 (Cat. No.03EX706), Indianapolis, IN, USA, 2003, pp 26–33
[36] Chen H Z, Zhang Y Y, Gong X and Xiang H 2014 *J. Phys. Chem. C* **118** 2333
[37] Yang J, Zhou J, Liu L and Li Y 2009 *Comput. & Math. Appl.* **57** 1995
[38] Lalwani S, Singhal S, Kumar R and Gupta N 2013 *Trans. Comb.* **2** 39
[39] Coello C A C, Pulido G T and Lechuga M S 2004 *IEEE Trans. Evol. Comput.* **8** 256
[40] Wang Y and Ren J 2020 *Phys. Chem. Chem. Phys.* **22** 4481
[41] Deb K, Pratap A, Agarwal S and Meyarivan T 2002 *IEEE Trans. Evol. Comput.* **6** 182
[42] Perdew J P, Burke K and Ernzerhof M 1996 *Phys. Rev. Lett.* **77** 3865
[43] Blöchl P E 1994 *Phys. Rev. B* **50** 17953
[44] Kresse G and Furthmüller J 1996 *Phys. Rev. B* **54** 11169
[45] Togo A, Oba F and Tanaka I 2008 *Phys. Rev. B* **78** 134106
[46] Madsen G K and Singh D J 2006 *Comput. Phys. Commun.* **175** 67
[47] Núñez-Valdez M, Allahyari Z, Fan T and Oganov A R 2018 *Comput. Phys. Commun.* **222** 152
[48] Zhang Y Y, Gao W, Chen S, Xiang H and Gong X G 2015 *Comput. Mater. Sci.* **98** 51
[49] Zhang L C, Qin G, Fang W Z, Cui H J, Zheng Q R, Yan Q B and Su G 2016 *Sci. Rep.* **6** 19830
[50] Cahangirov S, Topsakal M, Aktürk E, Şahin H and Ciraci S 2009 *Phys. Rev. Lett.* **102** 236804
[51] von Rohr F O, Ji H, Cevallos F A, Gao T, Ong N P and Cava R J 2017 *J. Am. Chem. Soc.* **139** 2771
[52] Kamal C and Ezawa M 2015 *Phys. Rev. B* **91** 085423
[53] Carrete J, Li W, Lindsay L, Broido D A, Gallego L J and Mingo N 2016 *Mater. Res. Lett.* **4** 204
[54] Liu D, Every A G and Tománek D 2016 *Phys. Rev. B* **94** 165432
[55] Şahin H, Cahangirov S, Topsakal M, Bekaroglu E, Akturk E, Senger R T and Ciraci S 2009 *Phys. Rev. B* **80** 155453
[56] Shafique A and Shin Y H 2017 *Sci. Rep.* **7** 506
[57] Dewandre A, Hellman O, Bhattacharya S, Romero A H, Madsen G K and Verstraete M J 2016 *Phys. Rev. Lett.* **117** 276601
[58] Pei Y, Shi X, LaLonde A, Wang H, Chen L and Snyder G J 2011 *Nature* **473** 66
[59] Liu W, Tan X, Yin K, Liu H, Tang X, Shi J, Zhang Q and Uher C 2012 *Phys. Rev. Lett.* **108** 166601
[60] Heremans J P, Jovovic V, Toberer E S, Saramat A, Kurosaki K, Charoenphakdee A, Yamanaka S and Snyder G J 2008 *Science* **321** 554
[61] Wang H, Pei Y, LaLonde A D and Snyder G J 2012 *Proc. Natl. Acad. Sci. USA* **109** 9705
[62] Ohta H, Kim S, Mune Y, Mizoguchi T, Nomura K, Ohta S, Nomura T, Nakanishi Y, Ikuhara Y, Hirano M *et al.* 2007 *Nat. Mater.* **6** 129
[63] Kuroki K and Arita R 2007 *J. Phys. Soc. Jpn.* **76** 083707
[64] Mahan G and Sofo J 1996 *Proc. Natl. Acad. Sci. USA* **93** 7436
[65] Pei Y, Wang H and Snyder G J 2012 *Adv. Mater.* **24** 6125
[66] Ding G, Li J and Gao G 2015 *RSC Adv.* **5** 91974
[67] Yan J, Gorai P, Ortiz B, Miller S, Barnett S A, Mason T, Stevanović V and Toberer E S 2015 *Energy & Environ. Sci.* **8** 983
[68] Guan J, Zhu Z and Tománek D 2014 *Phys. Rev. Lett.* **113** 046804
[69] Li L, Kim J, Jin C, Ye G J, Qiu D Y, Felipe H, Shi Z, Chen L, Zhang Z, Yang F *et al.* 2017 *Nat. Nanotechnol.* **12** 21
[70] Han W H, Kim S, Lee I H and Chang K J 2017 *J. Phys. Chem. Lett.* **8** 4627

Supporting Information: Directional Design of Two-Dimensional SnSe Materials with High Thermopower Based on the Pareto Optimization

Shenshen Yan[1], Yi Wang[1], Zhibin Gao[1,2], Yang Long[1], and Jie Ren[1,3]*
[1]*Center for Phononics and Thermal Energy Science, China-EU Joint Lab on Nanophononics, Shanghai Key Laboratory of Special Artificial Microstructure Materials and Technology, School of Physics Science and Engineering, Tongji University, Shanghai 200092, China*
[2]*Department of Physics, National University of Singapore, Singapore 117551, Republic of Singapore and*
[3]*Shanghai Research Institute for Intelligent Autonomous Systems, Tongji University, Shanghai 200092, China*
(Dated: January 19, 2021)

I. CORRELATION BETWEEN BAND EFFECTIVE MASS AND DENSITY OF STATES EFFECTIVE MASS, AND SEEBECK COEFFICIENT FOR 3D AND 2D MATERIALS

Here, we show the different correlations between Seebeck coefficient and density of states (DOS) effective mass (m^*_{DOS}) for 3D and 2D materials. Meanwhile, we can also obtain the correlations between band effective mass (m^*_{band}) and density of states (DOS) effective mass (m^*_{DOS}) for 3D and 2D materials.

According to the Onsager reciprocal relations of the charge and heat currents [1]: $j_q = L^{(0)} \cdot \mathbf{E} + \frac{L^{(1)}}{qT} \cdot (-\nabla T)$, $j_Q = \frac{L^{(1)}}{q} \cdot \mathbf{E} + \frac{L^{(2)}}{q^2 T} \cdot (-\nabla T)$, where $L^{(\alpha)} = q^2 \int \sigma(E)(E - E_F)^\alpha (-\frac{\partial f(E)}{\partial E}) dE$, we can obtain the electronic conductivity and the Seebeck coefficient under the parabolic band model approximation: $\sigma_0 = L^{(0)}, S = \frac{1}{qT}\frac{L^{(1)}}{L^{(0)}}$, where the q, $\mathbf{E}$, E, T, E_F and $f(E)$ are the charge , electric field, energy, temperature, Fermi energy and Fermi-Dirac distribution function, respectively.

When only considering the electronic transport near the Fermi level, after performing a Sommerfeld expansion, we can obtain the Mott's relations [2]: $S = \frac{\pi^2 k_B^2 T}{3q} \frac{d[ln(\sigma(E))]}{dE}\Big|_{E=E_F}$. We can find that the DOS will make an important effect on the Seebeck coefficient.

The $\sigma(E)$ is the energy-dependent electronic conductivity, expressed as: $\sigma(E) = \tau(E)v^2(E)G(E)$, where the $\tau(E)$, $v(E)$ and $G(E)$ are the electronic relaxation time, group velocity of carriers and DOS of multiple degenerate bands. The DOS of multiple degenerate bands, $G(E)$ is determined by the DOS of single band: $G(E) = N_v g(E)$, where the N_v and $g(E)$ are band degeneracy and the DOS of single band respectively. If only considering the acoustic phonon scattering, we can get: $\tau(E) \propto E^{-1/2}$ [3]. According to the free electron approximation, the correlation between group velocity of carriers and energy is $v(E) \propto E^{1/2}$. Here we will give the DOS expression for 3D and 2D systems.

For 3D system, the DOS of single band model is: $g_{3D}(E) = \frac{1}{2\pi^2}(\frac{2m^*_{band}}{\hbar^2})^{3/2}E^{1/2}$ where $\hbar$ is reduced Planck constant. If considering the multiple degenerate bands model, the DOS of multiple degenerate bands model, $G_{3D}(E)$ is: $G_{3D}(E) = \frac{1}{2\pi^2}(\frac{2m^*_{DOS}}{\hbar^2})^{3/2}E^{1/2} = N_v g_{3D}(E)$. Then we can obtain that: $G_{3D}(E) = \frac{2}{2\pi^2}(\frac{2N_v^{2/3}m^*_{band}}{\hbar^2})^{3/2}E^{1/2}$. Therefore, we can find the correlation among the DOS effective mass, band degeneracy and single band effective mass for the 3D system[4, 5]: $m^*_{DOS} = N_v^{2/3} m^*_{band}$.

Similarly, for 2D system, the DOS of single band model is: $g_{2D}(E) = \frac{2}{(2\pi)^2}\frac{2\pi}{\hbar}m^*_{band}$. If considering the multiple degenerate bands model, the DOS of multiple degenerate bands model, $G_{2D}(E)$ is: $G_{2D}(E) = \frac{2}{(2\pi)^2}\frac{2\pi}{\hbar}m^*_{DOS} = N_v g_{2D}(E)$. Hence, we also can obtain that: $G_{2D}(E) = \frac{2}{(2\pi^2)}\frac{2\pi}{\hbar}N_v m^*_{band}$. We can also find the correlation among the DOS effective mass, band degeneracy and single band effective mass for the 2D system: $m^*_{DOS} = N_v m^*_{band}$. Then, we give the formulas of the Seebeck coefficient for 3D and 2D systems.

For 3D system, the energy-dependent electronic conductivity: $\sigma_{3D}(E) \propto E$, we could obtain the Seebeck coefficient:

*Xonics@tongji.edu.cn

$$
\begin{aligned}
S_{3D} &= \frac{\pi^2 k_B^2 T}{3q} \frac{d[ln(\sigma(E))]}{dE}\Big|_{E=E_F} \\
&= \frac{\pi^2 k_B^2 T}{3q} \frac{1}{E_F} \\
&= \frac{\pi^2 k_B^2 T}{3q} \frac{2m^*_{DOS,F}}{\hbar^2 k^2_{3D,F}} \\
&= \frac{2\pi^2 k_B^2 T}{3q\hbar^2} (\frac{1}{3\pi^2 n})^{2/3} m^*_{DOS,F}
\end{aligned}
\tag{1}
$$

where $m^*_{DOS,F} = \frac{\hbar^2 k_F^2}{2E_F}$ is the DOS effective mass at the Fermi energy level, k_F is the Fermi radius, the $k_{3D,F} = (3\pi^2 n)^{1/3}$ is the Fermi radius for 3D system, and n is carrier concentration.

Similarly, for 2D system, the energy-dependent electronic conductivity: $\sigma_{2D}(E) \propto E^{1/2}$, we could obtain the Seebeck coefficient:

$$
\begin{aligned}
S_{2D} &= \frac{\pi^2 k_B^2 T}{3q} \frac{d[ln(\sigma(E))]}{dE}\Big|_{E=E_F} \\
&= \frac{\pi^2 k_B^2 T}{3q} \frac{1}{2} \frac{1}{E_F} \\
&= \frac{\pi^2 k_B^2 T}{3q} \frac{1}{2} \frac{2m^*_{DOS,F}}{\hbar^2 k^2_{2D,F}} \\
&= \frac{\pi k_B^2 T}{6qn\hbar^2} m^*_{DOS,F}
\end{aligned}
\tag{2}
$$

where the $k_{2D,F} = (2\pi n)^{1/2}$ is the Fermi radius for 2D system.

II. THE THERMOPOWER ALONG X AND Y DIRECTIONS

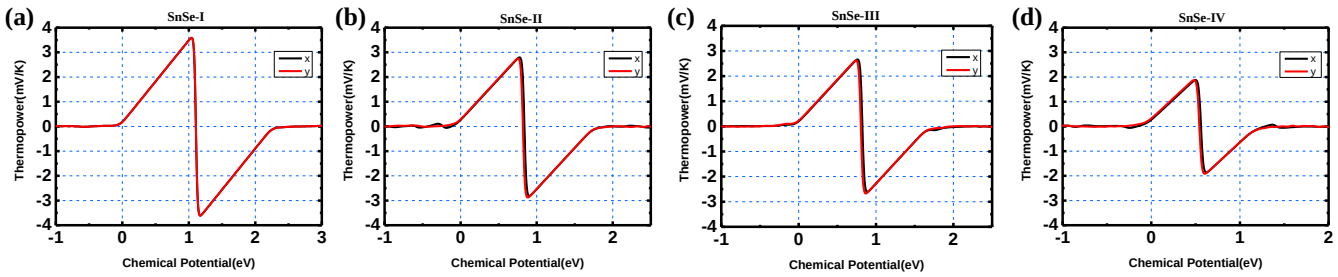

FIG. 1: There is thermopower of the four structures along x(black line) and y(red line) directions at 300K.

III. THE BILAYER STRUCTURES ON THE FIRST PARETO FRONT

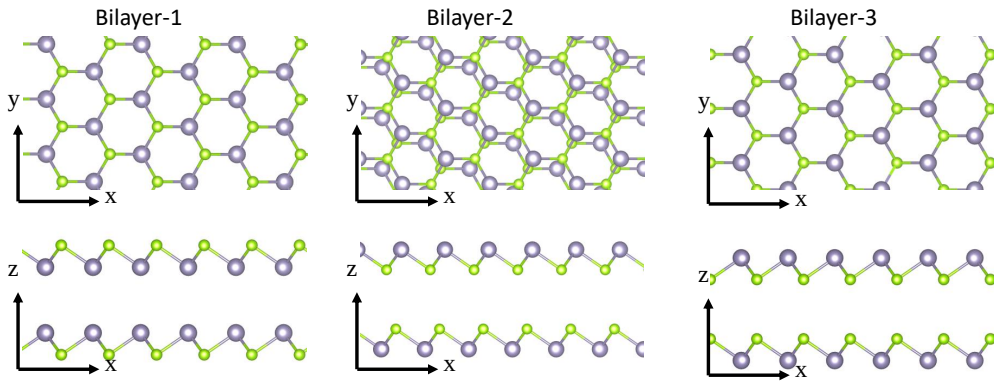

FIG. 2: There are three bilayer structures of 2D SnSe with the top and side views, which are blue hollow hexagonal symbols, as shown on the first Pareto Front.

TABLE I: Properties of three bilayer structures of 2D SnSe. There are space group, the values of lattice parameters a and b, free energy per atom and the values of thermopower, respectively.

Materials	Space group	a(Å)	b(Å)	E(eV/atom)	S(mV/K)
Bilayer-1	P-6m2	3.920	3.920	-4.081	2.829
Bilayer-2	P-1	3.913	3.915	-4.080	2.965
Bilayer-3	P-6m2	3.910	3.910	-4.079	2.968

IV. STRUCTURES ON THE SECOND PARETO FRONT AND THIRD PARETO FRONT

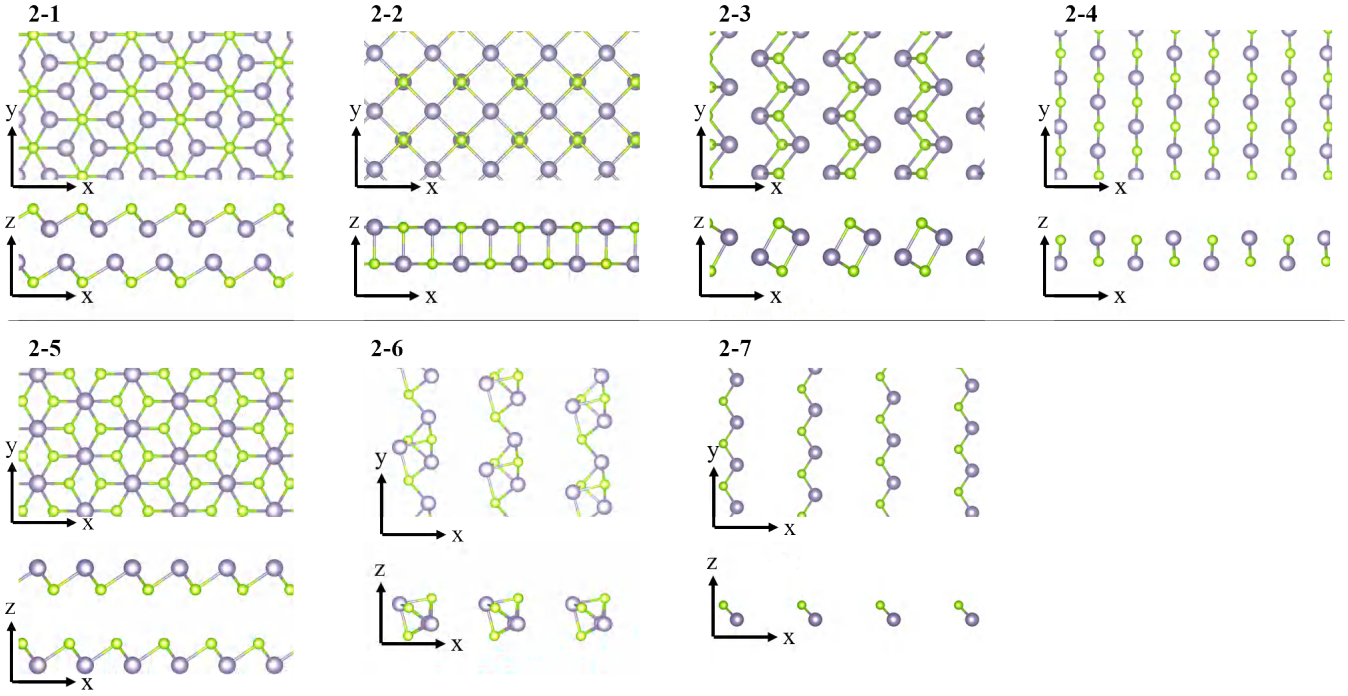

FIG. 3: Structures of 2D SnSe on the second Pareto Front are sorted by the free energy.

TABLE II: Properties of 2D SnSe structures on the second Pareto Front. There are space group, the values of lattice parameters a and b, free energy per atom and the values of thermopower, respectively.

Materials	Space group	a(Å)	b(Å)	E(eV/atom)	S(mV/K)
2-1	P-3m1	4.094	4.094	-4.137	0.887
2-2	Cmcm	4.320	4.320	-4.135	1.320
2-3	P-1	4.112	5.109	-4.105	1.555
2-4	Ama2	3.937	6.148	-4.103	2.719
2-5	C2/m	6.795	3.918	-4.080	2.906
2-6	P1	7.031	7.329	-3.990	2.914
2-7	P1	3.800	7.134	-3.794	2.971

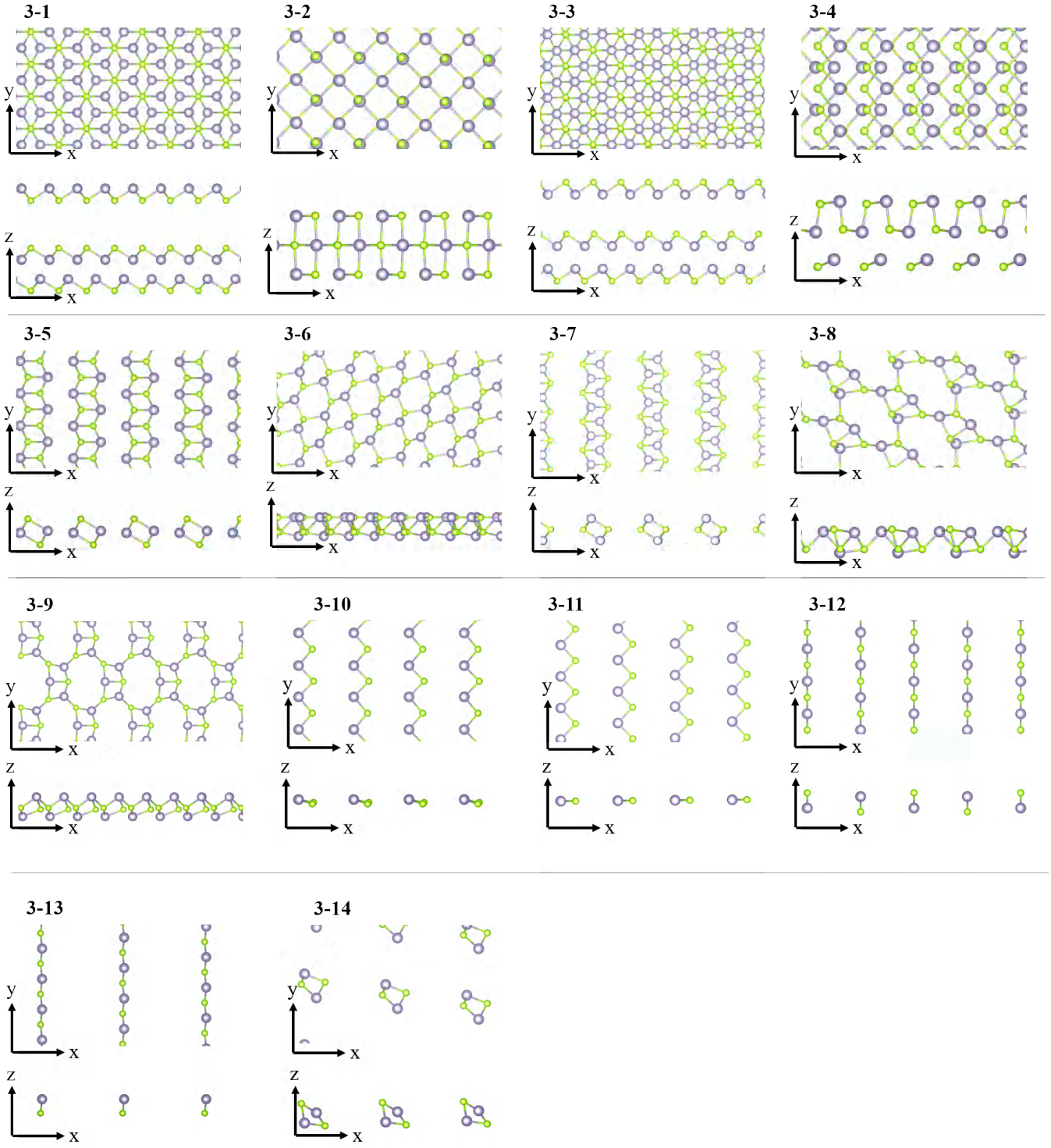

FIG. 4: Structures of 2D SnSe on the third Pareto Front are sorted by the free energy.

TABLE III: Properties of 2D SnSe structures on the third Pareto Front. There are space group, the values of lattice parameters a and b, free energy per atom and the values of thermopower, respectively.

Materials	Space group	a(Å)	b(Å)	E(eV/atom)	S(mV/K)
3-1	P3m1	4.039	4.039	-4.110	0.961
3-2	Cm	6.154	6.039	-4.107	1.003
3-3	Cm	6.825	3.989	-4.096	1.054
3-4	Pm	4.532	4.134	-4.077	1.359
3-5	P-1	3.911	6.410	-4.071	2.178
3-6	P1	6.516	6.501	-4.047	2.279
3-7	P-1	3.955	7.964	-4.034	2.720
3-8	P1	6.109	7.060	-4.027	2.762
3-9	P1	7.224	7.232	-3.986	2.775
3-10	Pm	6.594	7.615	-3.801	2.778
3-11	Amm2	3.793	13.768	-3.800	2.813
3-12	Pmmn	3.789	12.448	-3.797	2.894
3-13	P1	3.816	10.770	-3.787	2.963
3-14	P1	8.306	9.612	-3.738	2.970

[1] M. J. V. G. K. H. Madsen, J. Carrete, Comput. Phys. Commun. **231**, 140 (2018).
[2] G. Mahan and J. Sofo, Proc. Natl. Acad. Sci. U.S.A. **93**, 7436 (1996).
[3] V. I. K. A. S. G. D. L. Young, T. J. Coutts and W. P. Mulligan, J. Vac. Sci. Technol. **18**, 2978 (2000).
[4] T.-R. Wei, G. Tan, X. Zhang, C.-F. Wu, J.-F. Li, V. P. Dravid, G. J. Snyder, and M. G. Kanatzidis, J. Am. Chem. Soc. **138**, 8875 (2016).
[5] Z. M. Gibbs, F. Ricci, G. Li, Z. Hong, K. Persson, G. Ceder, G. Hautier, A. Jain, and G. J. Snyder, NPJ Comput. Mater. **3**, 1 (2017).